

Analysing the *Suzaku* Spectra of the Broad-Line Seyfert 1 Galaxy CBS 126

Chia-Ying Chiang^{1*}, R. C. Reis^{1,2}, A. C. Fabian¹, D. Grupe³ and S. Tsuruta⁴

¹*Institute of Astronomy, University of Cambridge, Madingley Road, Cambridge CB3 0HA*

²*Department of Astronomy, University of Michigan, Ann Arbor, MI 48109, USA*

³*Department of Astronomy and Astrophysics, Pennsylvania State University, 525 Davey Lab, University Park, PA 16802, USA*

⁴*Department of Physics, Montana State University, Bozeman, MT 59717, USA*

Accepted 2012 June 15. Received 2012 June 14; in original form 2011 October 25

ABSTRACT

We analysed new simultaneous *Suzaku* and *Swift* data of the Broad Line Seyfert 1 (BLS1) galaxy CBS 126. A clear Fe emission line and a strong soft excess are present in the source spectra. We fit the spectra with a relativistic reflection model and find the model tends to fit the data with a high iron abundance possibly due to the large soft excess present. By checking the difference and the RMS spectra, we find there is likely an absorption edge at ~ 0.89 keV, which might be caused by oxygen or neon. We also produced an analysis of the time-resolved spectra in order to examine the existence of the edge. Although high iron abundance is required more in the time-resolved spectra, a model of solar iron abundance together with an absorption edge gives a more physical explanation. Variation of the ionisation parameter is an alternative, plausible explanation for the excess seen in the difference spectra. It is difficult to know if there are warm absorbers in this source from the current data. To further investigate the presence of possible warm absorbers, higher signal-to-noise low-energy data are needed. The work presented here tentatively suggests that the spectra of a BLS1 can be explained by a relativistic reflection model similar to that often seen in their narrow-line cousins.

Key words: accretion,

1 INTRODUCTION

Broad-line Seyfert 1 galaxies (BLS1s) are a subclass of Active Galactic Nuclei (AGN) with broad permitted optical emission lines ($H\beta$ FWHM ≥ 3000 km s⁻¹). Unlike narrow-line Seyfert 1 galaxies (NLS1s; $H\beta$ FWHM < 2000 km s⁻¹), the broad-line region (BLR) of a BLS1 is of high velocity and close to the central black hole. Studies of Boller et al. (1996) concluded that high-velocity and steep soft X-ray continuum slopes are not found in nature in AGN population. The steep, ultrasoft X-ray spectra in NLS1s are generally believed to be because of a relatively low-mass black hole with a very high accretion rate (Pounds et al. 1995) or distant BLR clouds (Puchnarewicz et al. 1992).

CBS 126 (= Ton 1187, $\alpha_{2000} = 10^{\text{h}} 13^{\text{m}} 03.2^{\text{s}}$, $\delta_{2000} = +35^{\circ} 51' 24''$, $z = 0.079$) is a broad line Seyfert 1 galaxy with $H\beta = 2980 \pm 200$ km s⁻¹ (Grupe et al. 2004). It was detected as a bright X-ray AGN during the *ROSAT* All-Sky Survey (RASS, Voges et al. 1999) in 1990 November (Grupe et al. 1998a) and was observed again by *ROSAT* with the High Resolution Imager in 1995 October (Grupe et al. 2001). Our attention was drawn to CBS 126 because it shows a relatively high degree of optical continuum polarisation.

Grupe et al. (1998b) measured a degree of polarisation 1.26 ± 0.13 per cent, which is quite unusual for a soft X-ray selected AGN. The presence of optical polarisation suggests that part of the direct view is absorbed/reddened. Brandt et al. (1997) suggested and found that soft X-ray selected, highly polarised AGN show warm, ionised absorber in X-rays. CBS 126 is therefore a good candidate for finding ionised X-ray absorber features. It was again observed in X-rays as part of a *Swift* fill-in project to study the spectral energy distributions of AGN (Grupe et al. 2010) in 2006 June. The source shows similar properties to NLS1s such as strong spectral variability (see Fig. 1) and a large soft excess below ~ 1 keV, which are typical for NLS1s but unusual for BLS1s. CBS 126 harbours a black hole with an estimated mass in excess of $\sim 7.6 \times 10^7 M_{\odot}$ (Shen et al. 2011, SDSS DR7 catalogue). This, together with the high-velocity BLR clouds and the enormous soft excess make CBS 126 an interesting source.

A soft excess below ~ 1 keV is commonly seen in X-ray spectra of AGNs. It can be fitted phenomenologically by a blackbody with a temperature of $\sim 0.1 - 0.2$ keV, but the temperature of the component is fairly constant between sources, and is probably not related to the luminosity or black hole mass of the source (Gierliński & Done 2004). Instead, it is likely to have an atomic origin. Since the disc model predicts that the disc temperature should

* E-mail: cychiang@ast.cam.ac.uk

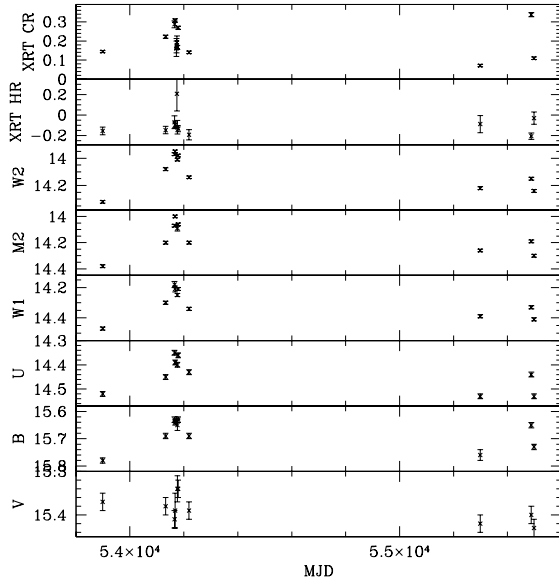


Figure 1. The figure shows the light curves of *Swift* instruments. The top two panels show the XRT count rate and hardness ratio, and the other panels show data extracted from different bands of UVOT data. We define the hardness ratio as $HR=(H-S)/(H+S)$ where S and H are the background-corrected number of counts in the 0.3-1.0 and 1.0-10.0 keV energy bands, respectively.

be correlated with the black hole mass, the soft excess is less likely to be due to the thermal emission from the accretion disc, except for objects with low black hole masses and high Eddington ratios such as NLS1s. Gierliński & Done (2004, 2006) suggested that soft excess can be caused by relativistically smeared and partially ionised absorption, but in this scenario an extreme outflow velocity is needed to produce a smooth spectrum (Schurch & Done 2007). Done et al. (2012) claimed that if the inner disc emission emerges as a Comptonisation component rather than a blackbody spectrum, the Wien tail of this component could produce the soft excess. Jin et al. (2012) showed that the model could explain the spectra of a sample of unobscured type 1 AGNs. This scenario requires an electron population with a relatively low temperature and high optical depth, and the Compton upscattering component to arise in the transition region between the disc and the corona. It again requires an unexplained, fairly constant temperature between sources.

An alternative physical interpretation to explain the broadband X-ray spectrum is the relativistic reflection model. Crummy et al. (2006) investigated a large sample of type 1 AGNs and found the relativistically blurred reflection can reproduce the soft excess. The soft excess here is a series of blurred emission lines caused by disc reflection and other emission (Ross & Fabian 2005). The constancy of the shapes is then due to atomic physics.

One of the major goals in observing CBS 126 with *Suzaku* and *Swift* simultaneously, was to clarify the nature of its unusual, variable, optically polarised spectrum as found from earlier *Swift* observations. Fig. 1 exhibits correlated variability in the optical/UV and X-ray bands. Most importantly, the earlier *Swift* data already showed that the variability in the X-ray band itself takes place mostly at higher energies, while at the lower X-ray energies there was no significant variability. Furthermore, earlier *Swift* data exhibited steep soft X-ray spectra during dimmer states while flatter spectra during higher states. Standard accretion disc-corona mod-

Table 1. Summary of the *Suzaku* observations of CBS 126. The 0.5-10 keV net source count rates for different detectors are listed below.

Detector	window	MJD	Exposure	Count Rate
XIS0	3 × 3	55487.358	72505	0.367 ± 0.002
	5 × 5	55487.831	29061	0.339 ± 0.003
XIS1	3 × 3	55487.358	72481	0.811 ± 0.003
	5 × 5	55487.831	29061	0.743 ± 0.005
XIS3	3 × 3	55487.358	72505	0.404 ± 0.002
	5 × 5	55487.831	29061	0.378 ± 0.004

els cannot explain this kind of behaviour. For instance, those models would expect the soft X-rays to vary in a similar manner to the hard X-rays, i.e. the variety would be broadband in X-rays, which is not the case with CBS 126. On the other hand, the spectral and temporal behaviour of this source can be *well explained* with ionised relativistic reflection models (Miniutti & Fabian 2004). In this picture the relativistic reflection component, including the soft X-ray excess, dominates during dimmer states, and thus give rise to the observed steep soft X-ray spectra. In contrast, during brighter states, the reflection component is diluted and the flatter powerlaw dominates. The focus of this paper is to test whether our new simultaneous *Suzaku/Swift* data further support the relativistic reflection model for CBS 126. Other possibilities will not be probed in depth.

2 DATA REDUCTION

2.1 *Suzaku*

CBS 126 was observed by *Suzaku* on 2010 October 18 for a total of ~ 100 ks of good exposure time (see Table 1). The X-ray Imaging Spectrometer (XIS) was operated in the normal mode. All the detectors (XIS0, XIS1 and XIS3) were operated in both 3×3 and 5×5 editing modes. We reduced the data with the HEASOFT V6.10 software package following the *Suzaku* Data Reduction Guide. We used a circle with a 180 arcsec diameter to extract the source spectrum. The background spectrum was extracted using the same size of circular region from a position free from the source, the calibration source and any other clear cosmic source. Response files were produced by the script XISRESP, which calls XISRMPGEN and XISSIMARFGEN automatically. Spectra and response files of the two front-illuminated (FI) CCD XIS detectors (XIS0 and XIS3) were combined using the script addascaspec in FTOOL, resulting in a total 2 - 10 keV flux of which is 4.12×10^{-12} ergs $\text{cm}^{-2} \text{s}^{-1}$. The XIS 0.5-10.0 keV light curve of CBS 126 is shown in the upper panel in Fig. 2. It is clear that the XIS light curve is variable. We also produced the difference spectrum by subtracting the low-flux state spectrum from the high-flux state spectrum. The XIS light curve was divided into two flux intervals, both having a similar number of counts. The slice above the average count rate (1.25 ct/s for XIS FI and 2.00 ct/s for XIS BI) forms the high-flux state spectrum, while the slice below the average represents the low flux spectrum. The total 0.5 - 2 keV fluxes are 4.57×10^{-12} ergs $\text{cm}^{-2} \text{s}^{-1}$ and 4.49×10^{-12} ergs $\text{cm}^{-2} \text{s}^{-1}$ for XIS FI and back-illuminated (BI, that is, XIS1) spectra, respectively.

The Hard X-ray Detector (HXD) was operated in XIS-nominal pointing mode. The background spectrum of HXD/PIN consists of a non-X-ray background and a cosmic X-ray background. We obtained the non-X-ray background event file from a database of background observations made by the PIN diode. The

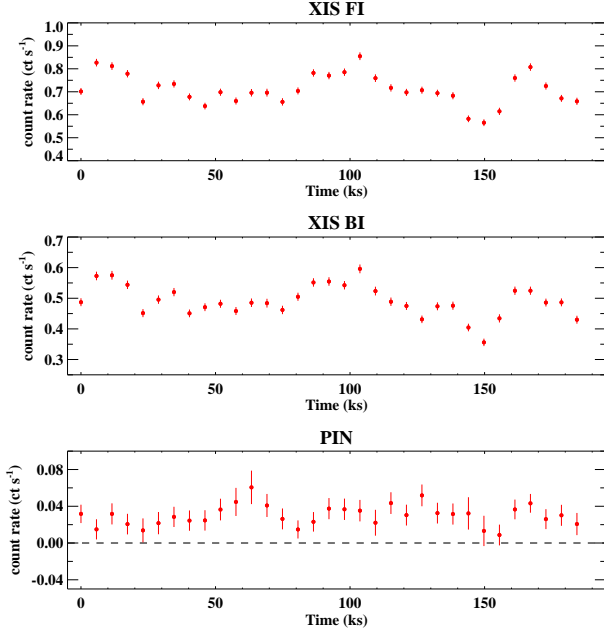


Figure 2. The figure shows the background-corrected light curves of FI and BI XIS detectors, and PIN data. These light curves have been binned to orbital bins (5760 s) for clarity.

background model D (the tuned model) was used for non-X-ray background extraction. The cosmic X-ray background was estimated by model simulation using the PIN response for flat emission distribution, and the count rate in this case is 0.187 ± 0.001 counts s^{-1} in the effective PIN energy band 14.0–45.0 keV (all the count rates of PIN will be given over this band if not specified). The source is faint (0.328 ± 0.002 counts s^{-1}), appearing at only ~ 4 percent above the background level (0.316 ± 0.001 counts s^{-1}). Since the background dominates the PIN spectrum, we produced the earth-occulted background for a further check. Ideally the earth-occulted background should be identical to the non-X-ray background. The counts of the earth-occulted background (0.358 ± 0.004 counts s^{-1}) are however slightly higher (~ 15 percent) than that of the non-X-ray background (0.298 ± 0.001 counts s^{-1}), which means the PIN data were mildly over-estimated. The navy blue points in Fig. 3 is the total background including the earth-occulted background and the cosmic background, and the cyan points slightly below stand for the PIN spectrum before background correction. It can be seen that if we replace the non-X-ray background with the earth-occulted background, we effectively have a non-detection in the PIN band. The green points in Fig. 3 are the background-corrected PIN data when using the non-X-ray background. Since the data show no solid detection in PIN, we do not include the PIN spectrum in all our spectral fittings. The light curve plotted in the lower panel of Fig. 2 also shows the source is faint in the PIN energy band, thus we did not generate a difference spectrum for PIN either.

2.2 Swift

The *Swift* Gamma-Ray Burst (GRB) explorer mission (Gehrels et al. 2004) observed CBS 126 13 times. Note that some of these observations were very short due to *Swift* triggers on Gamma Ray Bursts. A summary of all *Swift* observations between 2006 June 13 and 2010 October 29 is given in Table 2.

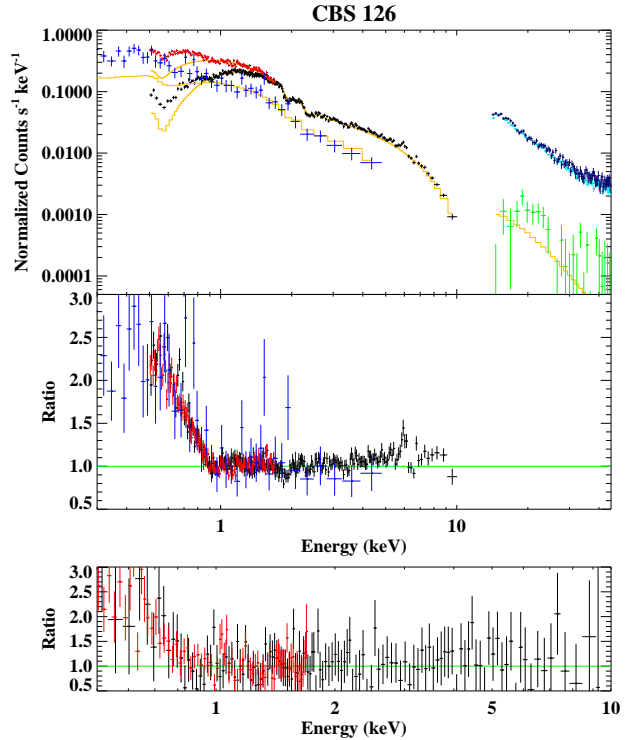


Figure 3. The top panel shows the overall spectra fitted with a powerlaw across the 0.9 to 4 keV and 7.5 to 10 keV energy range. We show the FI XIS and BI XIS spectra in black and red respectively. The PIN spectrum is shown in green and the *Swift* XRT spectrum is shown in blue. The navy, blue and cyan data are explained in detail in section 2.1. A strong soft excess at low energies and iron line structure can be clearly seen. The lower panel shows the data/model ratio of the difference spectra (see definition in section 2.1) with the same powerlaw model applied. The BI XIS difference spectrum above 1.7 keV and the FI XIS above 10 keV are ignored due to poor signal-to-noise.

We use *Swift* data taken simultaneously with the above *Suzaku* observation. The *Swift* X-Ray Telescope (XRT; Burrows et al. 2005) was operating in photon counting mode (PC mode; Hill et al. 2004) and the data were reduced by the task *xrtpipeline* version 0.10.4, which is included in the HEASOFT package 6.1. Source photons were selected in a circular region with a radius of $70''$ and background region of a close by source-free region with $r = 200''$. The background region is much larger than the source region in order to get enough counts to model the background spectrum. Photons were selected with grades 0–12. The photons were extracted with XSELECT version 2.4. The spectral data were re-binned by using *grppha* version 3.0.0 having 20 photons per bin. The spectra were analysed with XSPEC version 12.3.1 (Arnaud 1996) between 0.3 and 5 keV. The ancillary response function files (arfs) were created by *xrtmkarf* and corrected for vignetting and bad columns/pixels using the exposure maps. The standard response matrices *swxpc0to12s0_20010101v011.rmf* and *swxpc0to12s6_20010101v011.rmf* were used for the observations before and after the XRT substrate voltage change in 2007 August, respectively (Godet et al. 2009). The difference spectrum was not generated because the exposure time (~ 6 ks) is too short.

One of the advantages of *Swift* is that data are taken simul-

Table 2. Summary of the *Swift* observations of CBS 126. Start and end times T_{start} and T_{end} of the observations are given in UT and all exposure times are given in units of s. XRT Count rates and hardness ratios (HR) of CBS 126 are also displayed. The UVOT magnitudes were corrected for Galactic reddening ($E_{B-V} = 0.011$; Schlegel et al. 1998).

Segment	T_{start}	MJD	T_{XRT}	Count Rate	HR	V	B	UV W1	UV W2
001	2006-06-13 00:18	53899.010	4725	0.144 ± 0.006	-0.16 ± 0.04	15.37 ± 0.02	15.78 ± 0.01	14.47 ± 0.01	14.32 ± 0.01
002	2007-02-01 11:29	54132.476	4014	0.222 ± 0.008	-0.15 ± 0.04	15.38 ± 0.02	15.69 ± 0.01	14.30 ± 0.01	14.08 ± 0.01
003	2007-03-06 12:01	54165.499	913	0.288 ± 0.018	-0.07 ± 0.06	15.41 ± 0.02	15.63 ± 0.01	14.18 ± 0.02	13.97 ± 0.01
004	2007-03-08 13:18	54167.552	4977	0.307 ± 0.009	-0.09 ± 0.03	15.39 ± 0.04	15.64 ± 0.01	14.21 ± 0.02	13.95 ± 0.01
007	2007-03-13 07:58	54172.331	99	0.160 ± 0.040	—	—	—	—	—
008	2007-03-14 01:39	54172.999	125	0.175 ± 0.038	—	—	—	—	—
009	2007-03-15 14:36	54174.610	202	0.193 ± 0.033	$+0.21 \pm 0.16$	—	—	—	—
010	2007-03-17 08:05	54176.335	1782	0.166 ± 0.011	-0.12 ± 0.07	15.34 ± 0.03	15.65 ± 0.02	14.25 ± 0.01	14.01 ± 0.01
011	2007-03-20 08:27	54179.351	4266	0.269 ± 0.008	-0.13 ± 0.03	15.34 ± 0.02	15.63 ± 0.01	14.21 ± 0.01	13.98 ± 0.01
015	2007-04-29 08:55	54219.369	3069	0.141 ± 0.007	-0.19 ± 0.05	15.39 ± 0.02	15.69 ± 0.01	14.34 ± 0.01	14.14 ± 0.01
016	2010-04-13 02:15	55299.092	2608	0.072 ± 0.006	-0.09 ± 0.08	15.42 ± 0.02	15.76 ± 0.02	14.39 ± 0.01	14.22 ± 0.01
017	2010-10-19 08:30	55488.353	3160	0.337 ± 0.011	-0.21 ± 0.03	15.40 ± 0.02	15.65 ± 0.01	14.33 ± 0.01	14.15 ± 0.01
018	2010-10-29 01:14	55498.162	2986	0.111 ± 0.007	-0.03 ± 0.06	15.43 ± 0.02	15.73 ± 0.01	14.41 ± 0.01	14.24 ± 0.01

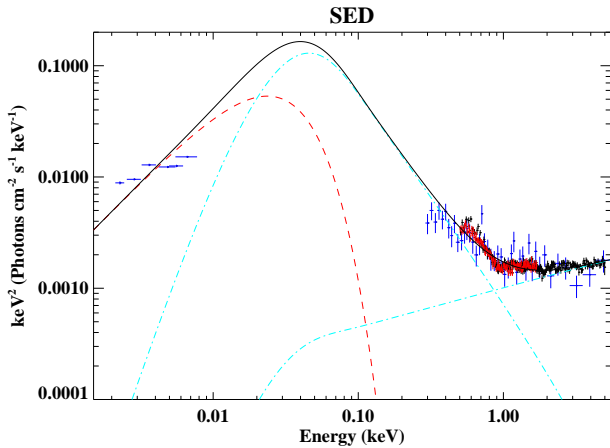


Figure 4. The figure shows the SED plot from the 17 (blue points) segment of *Swift* data which is simultaneous with our *Suzaku* observation. *Suzaku* XIS FI (black) and BI (red) data have been included for reference. The optical-X-ray connecting index α_{ox} is ~ 1.42 .

taneously in X-rays and in the Optical/UV. Therefore, data were also taken with the UV/Optical Telescope (UVOT; Roming et al. (2005)) using 6 photometry filters. Before analysing the data, the exposures of each segment were co-added by the UVOT task *uvotimsum*. Source counts were selected with the standard $5''$ radius in all filters (Poole et al. 2008) and background counts in a source-free region with a radius $r=20''$. The data were analysed with the UVOT software tool *uvotsource* assuming a GRB like power law continuum spectrum. The magnitudes as listed in Table 2 were all corrected for Galactic reddening $E_{B-V} = 0.011$ given by Schlegel et al. (1998). The correction factor in each filter was calculated with equation (2) in Roming et al. (2009) who used the standard reddening correction curves by Cardelli et al. (1989).

3 DATA ANALYSIS

We fit a powerlaw modified with Galactic absorption across the 0.9–4 keV and 7.5–10 keV energy ranges, and the results are shown in Fig. 3. A large soft excess in both FI and BI XIS spectra and the

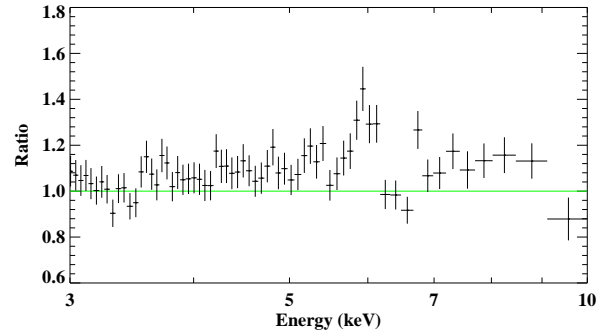


Figure 5. The figure shows ratio plot of the iron line profile of FI XIS spectrum. The equivalent width (EW) of the line is 114^{+35}_{-36} eV.

Swift XRT spectrum, and an iron emission line in the FI XIS spectrum can be clearly seen. We also fit the modified powerlaw model to the *Suzaku* difference spectra (see the lower panel of Fig. 3). The difference spectra are quite noisy due to lack of data. A simple powerlaw fits the difference spectra above 1 keV, and there are no features around the iron line band as expected if the features are due to constant, additive component such as an emission line. Despite poor signal-to-noise in the difference spectrum, soft excesses are still present, similar to that seen in the real spectra. This hints at the possibility of either a further distinct varying component acting preferentially in the low-energy band or the presence of a multiplicative component, as the latter is not removed in the difference spectra even if it does not change with time.

In the frame work of an extra component acting preferentially at low energies, the large soft excess could be due to a possible Comptonised Wien tail from the disc component. We investigate the possibility of this scenario by fitting the spectral energy distribution (SED) of the UV and soft X-ray data of CBS 126 with a Comptonisation model. The UV data have been fitted with a low-temperature blackbody disc component (DISKBB, Mitsuda et al. 1984). Two Comptonisation components (COMPTT, Titarchuk 1994) have been included to explain the soft excess and the powerlaw-shape spectrum at high energies. As shown in Fig. 4, the Comptonised Wien tail can reproduce the shape of the soft excess. If the component which produces the soft excess varies with the hard

Table 3. The table below lists the fitting parameters and χ^2 obtained by models fitted over different energies. Γ is the photon index of the powerlaw component, and N_{pow} stands for the normalisation of the powerlaw component. τ is the depth of the absorption edge. “Index” is for the emissivity profile index in the convolution model KDBLUR. N_{iref} and N_{nref} represent the normalisations of the ionised and neutral reflection components, respectively. In this table all the errors are at the 90% confidence level.

	Time-averaged		Time-resolved	
	Model A	Model B	Model A	Model B
Γ	2.01 ± 0.01	$2.16^{+0.01}_{-0.02}$	$2.00^{+0.02}_{-0.03}$	$2.11^{+0.03}_{-0.02}$
$N_{\text{pow}} (10^{-3})$	1.5 ± 0.1	1.4 ± 0.1	See Table 4	
E_{edge}	-	0.89 ± 0.01	-	$0.88^{+0.02}_{-0.01}$
τ	-	$0.35^{+0.02}_{-0.03}$	-	$0.39^{+0.05}_{-0.04}$
index	$7.2^{+0.8}_{-1.3}$	> 5.4	$4.2^{+0.3}_{-0.1}$	5.8 ± 2.1
$R_{\text{in}} (R_g)$	$3.0^{+0.6}_{-0.4}$	$1.7^{+0.6}_{-0.1}$	< 2.2	$1.7^{+0.5}_{-0.2}$
i	$27^{+20}_{-6} \circ$	$51^{+3}_{-14} \circ$	$< 19 \circ$	$51^{+11}_{-16} \circ$
A_{Fe}	> 9.0	(1.0)	> 9.5	(1.0)
ξ	200^{+12}_{-23}	119^{+33}_{-28}	See Table 4	
$N_{\text{iref}} (10^{-7})$	$2.5^{+0.6}_{-1.2}$	$6.2^{+3.4}_{-0.9}$	See Table 4	
$N_{\text{nref}} (10^{-6})$	$8.9^{+2.6}_{-2.5}$	$10.7^{+3.8}_{-4.1}$	8.7 ± 2.3	$11.0^{+5.1}_{-4.8}$
$\chi^2/d.o.f.$	1642/1476	1632/1475	1148/1067	1181/1066

powerlaw-shape component, the model could explain both the real and difference spectra. However, the possible iron emission feature present in the *Suzaku* FI XIS spectrum (see Fig. 5) with a line width of $0.12^{+0.07}_{-0.05}$ keV at ~ 6.41 keV (rest energy), though not significantly broadened, together with the large soft excess which could be caused by blurred reflection, act to validate the relativistic reflection scenario. As stated in the introduction, the purpose of the work is to test if the relativistic reflection model can explain the overall shape of the X-ray continuum of the new *Suzaku* observation. In what follows, we explore this possibility further, though it may not be the only explanation of the data as the Compton hump has not been detected by *Suzaku* PIN.

3.1 Time-averaged Spectra

We start by fitting the data with the simplest model that can explain the broad iron line in a physically consistent manner as well as the soft excess. The model consists of a reflection continuum model REFLIONX (Ross & Fabian 2005) convolved by the KDBLUR model. We also model the neutral reflection with REFLIONX by setting the ionisation parameter $\xi = 1.0$. The Galactic absorption is modelled by TBnew using Wilms (Wilms et al. 2000) abundance. The model (hereafter Model A) and the fitting parameters are summarised in Table 3.

It is found that the iron abundance A_{Fe} tends to be higher than 9 times of the solar value, which is not expected. If we set the iron abundance to be the same as the solar value, the $\chi^2/d.o.f.$ of the fitting increases to 2014/1477 and the model failed to reproduce the soft excesses below 0.9 keV. A blackbody component possibly arising from a low-temperature accretion disc was then considered, even though we do not expect the disc emission to change within such a short period of time and thus should not give rise to the soft excess seen in the difference spectrum. To examine whether the disc emission is present in the X-ray band and contributes variability, we generated the root mean square (RMS) spectrum using the

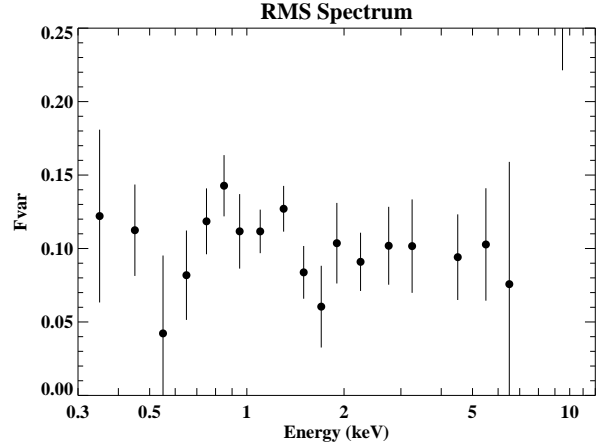


Figure 6. The figure shows the RMS spectrum of CBS 126. Each data point is calculated using a light curve with a time bin of 1ks. The last data point around 10 keV shows a much higher fraction of variability than the others possibly due to severe noise at the highest energy band.

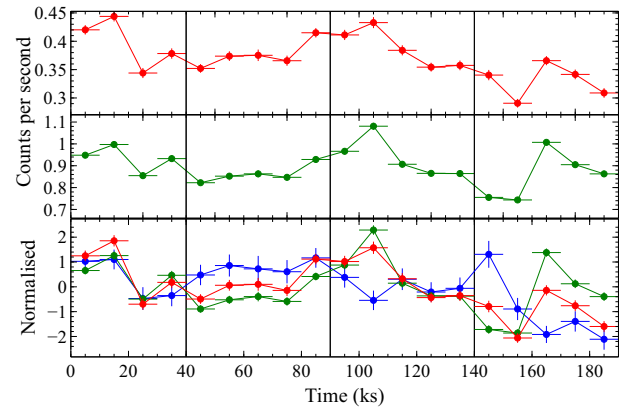


Figure 7. XIS light curve in the hard (1.0-10.0 keV; red) and soft (0.3-1.0 keV; green) energy band and colour evolution (soft/hard; blue). In the lower panel these were normalized by dividing the difference between the count rate in each 10 ks bin and the mean count rate by the standard deviation. See section 3.2 for detail.

technique developed by Edelson et al. (2002). The RMS spectrum of CBS126 (see Fig. 6) is flat, and the variability of each energy band lies on a similar level. This implies that not a particular energy band contributes significantly more variability than the other energy bands. Furthermore, when adding a DISKBB component to the spectra, an effective temperature T_{eff} of ~ 50 eV is required to explain the soft excess, which is way too high for a $M \sim 10^8 M_{\odot}$ black hole (typical value $T_{\text{eff}} \sim 10$ eV for black holes of this mass). Therefore, the possibility of a blackbody component can be ruled out and either the source has a highly supersolar iron abundance or there is a further component contributing to the soft excess which must also be present in the difference spectrum.

In order to test the possibility that the soft excess in the difference spectrum is due to a combination of reflection at solar abundances and a further multiplicative component, we added an absorption edge using ZEDGE to Model A and froze the iron abundance at solar. This model is hereafter referred to as Model B (Table 3). This resulted in a fit with similar quality ($\chi^2/d.o.f. =$

Table 4. The table below lists the fitting parameters of different periods of the observation obtained by the time-resolved analysis. Definitions of these parameters are identical with those shown in Table 3.

Time-resolved	P1	P2	P3	P4
Model A				
$N_{\text{pow}} (10^{-3})$	1.5 ± 0.1	1.4 ± 0.1	1.4 ± 0.1	1.3 ± 0.1
ξ	200^{+11}_{-42}	193^{+15}_{-49}	109^{+14}_{-6}	104^{+8}_{-11}
$N_{\text{iref}} (10^{-7})$	$3.1^{+1.2}_{-0.6}$	$3.3^{+1.0}_{-0.6}$	$12.1^{+3.3}_{-5.0}$	$12.1^{+1.9}_{-7.5}$
Model B				
$N_{\text{pow}} (10^{-3})$	1.5 ± 0.1	1.3 ± 0.1	1.5 ± 0.1	1.4 ± 0.1
ξ	208^{+28}_{-61}	208^{+24}_{-98}	103^{+34}_{+32}	90^{+31}_{-29}
$N_{\text{iref}} (10^{-7})$	$2.3^{+0.9}_{-0.6}$	$2.4^{+1.7}_{-0.6}$	$7.6^{+5.4}_{-3.6}$	$6.9^{+2.7}_{-1.2}$

1632/1475) to that of Model A when the iron abundance was > 9 . The energy of the absorption edge is ~ 0.89 keV, which is likely associated with oxygen or neon.

It is clear from Fig. 2 that the *Suzaku* XIS light curves are variable. In the following we extend our spectral analysis to time-resolved spectra.

3.2 Time-resolved Spectra

3.2.1 Spectral Fitting

A 0.3-1.0 keV and a 1.0-10.0 keV *Suzaku* XIS light curves with a 10 ks time bin were created and are shown in Fig. 7. The top two panels of Fig. 7 shows the “soft” (0.3-1.0 keV) and the “hard” (1.0-10.0 keV) light curves, respectively. The blue line in the lower panel shows the colour (the soft/hard ratio) evolution of the observation. When we look at the top two panels of Fig. 7, the count rates of the soft and the hard light curves appear to vary with each other. However, looking at the normalised colour evolution (soft/hard), it appears that there could in fact be at least four distinct periods which are highlighted by the vertical lines in Fig. 7. As such, we proceed by dividing the observation into these different segments and created a new set of time-resolved spectra. The observation was divided into the segments as follows: 0-40 ks (period 1), 40-90 ks (period 2), 90-140 ks (period 3) and 140-190 ks (period 4). The resulting *Suzaku* FI XIS spectra are noisy in the low-energy band (of particular interest to us since we are looking for the soft excess), therefore only the *Suzaku* low-energy BI XIS spectra were used. The *Swift* XRT spectrum has an exposure time much less than 40 ks and is not suitable for time-resolving analysis envisioned here.

We fit each time-resolved spectrum with both models A and B. The iron abundance, inclination, neutral hydrogen density, emissivity index, edge energy and inner radius are treated as global parameters and are tied between the periods (i.e., they are assumed to be constant at these time scales). The normalisation of the powerlaw and ionised reflection component, as well as the ionisation parameter of the inner disc, on the other hand, are free to vary. The normalisation of the neutral reflection component is also free to vary, but tied between the periods. Table 3 also summarises the results for the global parameters in the time-resolved data and Table 4 shows the evolution of the remaining parameters. Fig. 8 displays the data/model ratio for Model B, with the different periods shown in separate panels for clarity. It can be seen that that this model fits the spectra of each periods well, with no evidence for a soft excess. The energy of the absorption edge is found to be ~ 0.88 keV, which is consistent with that obtained by the time-averaged spectra.

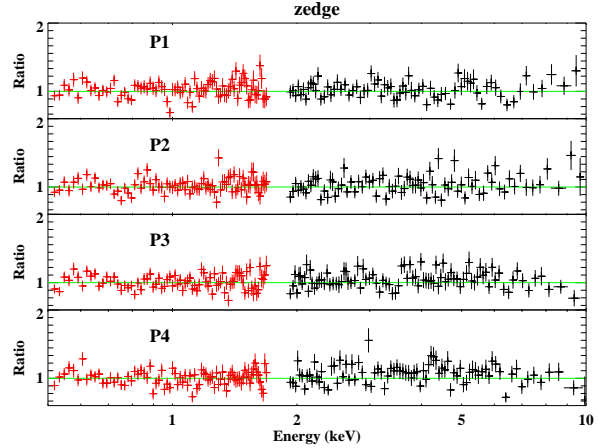


Figure 8. The figure shows the fitting results of spectra in different periods using model B. The black and red points represent FI and BI XIS data, respectively. The FI XIS spectra below 1.9 keV were ignored because the spectra turned to be noisy after breaking down into segments.

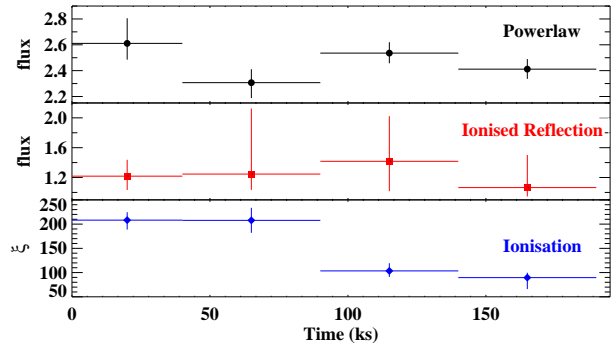


Figure 9. The figure shows, from top to bottom, the 0.01-1000 keV flux (in unit of 10^{-11} erg cm^{-2} s^{-1}) evolution of the powerlaw component, the ionised reflection component, and the evolution of the ionisation state. In this figure the error bars are of 1σ .

Based on our time-resolved analysis, we find that Model A, which still tends to give a high iron abundance, yields a better χ^2 in time-resolved spectra than Model B. This may be due to the lack of *Swift* spectra that offer a low energy coverage down to 0.3 keV. The resulting parameters of the time-resolved spectra are very similar to those obtained in the time-averaged spectra. The best-fitting values are not exactly the same but all agree within the 90% confidence level. The FI XIS and the *Swift* XRT spectra are not included in fitting the time-resolved spectra, so slightly different best-fitting results of parameters are expected.

3.2.2 Flux Variation

The top two panels of Fig. 9 show the variation in the 0.01-1000 keV flux level of the powerlaw and the ionised reflection components, and the bottom panel shows the variation in ionisation parameter of the reflection component. The ionisation parameter is defined as $\xi = L_{\text{ion}}/nR^2$, where L_{ion} is the ionising luminosity, n is the hydrogen number density, and R is the distance to the ionising source. ξ is proportional to the ionising luminosity, which in this case is coming from the powerlaw continuum. The flux of the

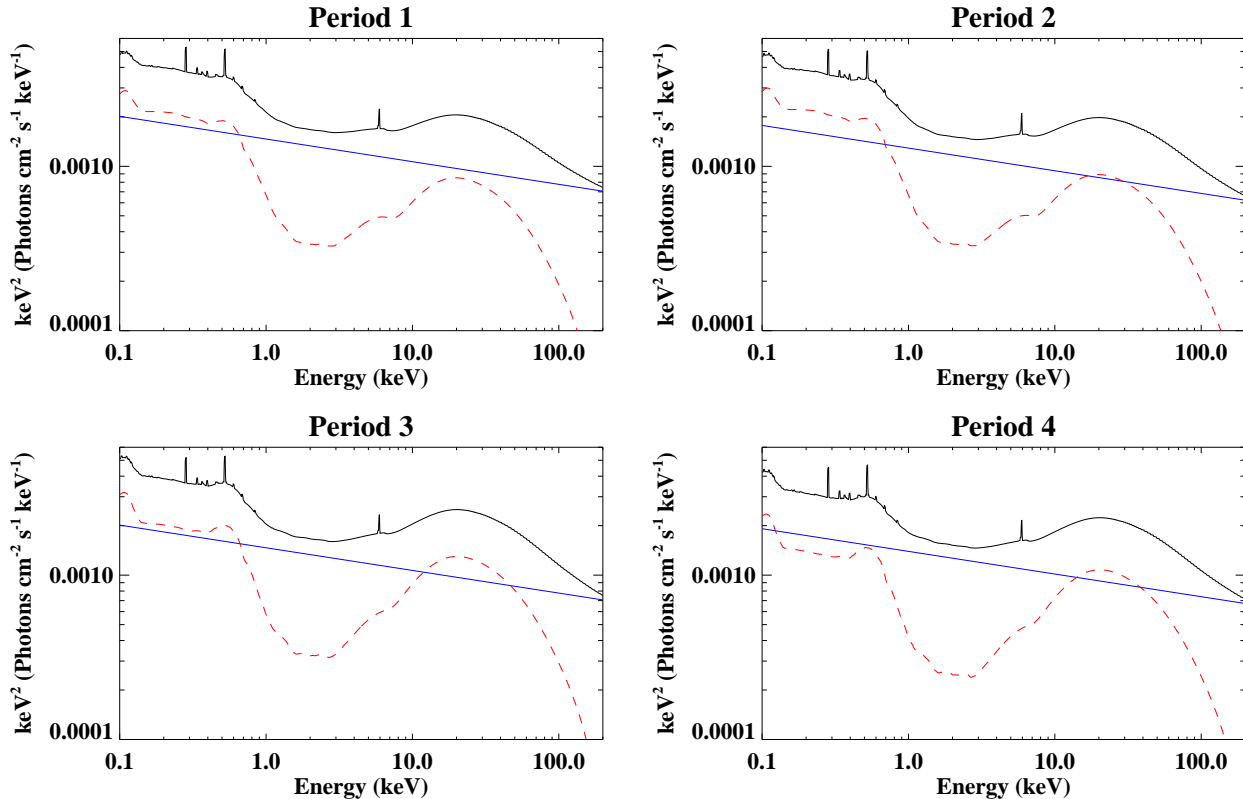


Figure 10. Each of the set of figures shows the decomposed components of model B in a period. The black line above shows the overall model without Galactic absorption and the edge. The blue line represents a $\Gamma = 2.11$ powerlaw. The red dash line shows the ionised reflection component. The neutral reflection component stays constant throughout the periods and is omitted for the purpose of clarity.

powerlaw component varies in time in a similar manner to the overall light curve (see Fig. 7) and is the dominant cause of flux variability in the source. This is often the case observed in Seyfert 1 galaxies (e.g. MCG-6-30-15). The ionised reflection flux, on the other hand, remains at a constant level within the uncertainties through the four periods. However, the evolution of ionisation parameter does not follow the trend laid out by the powerlaw component as expected from the $\xi = L_{\text{ion}}/nR^2$ definition of the ionisation parameter if the product nR^2 remains constant. Irrespective of which model is used, i.e. with or without the extra edge, the ionisation parameter decreases with time.

We depict the evolution of the powerlaw and the reflection components in Fig. 10. As the neutral reflection component is not expected to vary in these time scales, we only plot the unabsorbed reflection (ionised plus neutral) component together with the powerlaw continuum. From period 1 to period 2, the reflection component stays more or less constant but the powerlaw component drops. It can be seen that the drop in the powerlaw between periods 1 and 2 could, by itself, give rise to an apparent soft excess in the difference spectrum. The drop in the ionisation parameter in periods 3 and 4 causes the low energy part of the reflection to appear lower in comparison to the continuum. This would of course have the effect of producing an even stronger soft excess in the difference spectrum. It is clear from this qualitative description of the evolution of the reflection component that the soft excess seen in both the real and difference spectrum (as well as the broad iron line seen in Fig. 5)

could indeed be caused solely by the changes in the ionised reflector and powerlaw continuum.

We try to fit the *Suzaku* difference spectra presented in Fig. 3 with an absorbed powerlaw and an ionised reflection component. The parameters of the reflection component were set to be the same as those obtained for the time-averaged spectral analysis. We find that the simple model indeed fits the difference spectra well, indicating that the excess shown in the soft difference spectra could alternatively be caused by the change in the ionisation parameter. Interestingly, a similar conclusion was reached by Reis et al. (2012), where the authors find that changes in the ionisation parameter was necessary to explain the hard excess seen in the difference spectra of the Seyfert 1 galaxy NGC 3783. In that case, the hard excess were due to dramatic changes in the level of the Compton hump.

4 DISCUSSION

4.1 High Iron Abundance or Absorption Edge

The iron abundance in a galaxy can be super-solar if there is a high level of star formation. Some Seyfert I galaxies have super-solar abundances, for instance, 1H0707-495, which strongly requires abundances over eight times of solar value (Fabian et al. 2009). However, 1H0707-495 shows the distinct presence of a strong Fe-K (~ 970 eV) emission line as well as Fe-L emission (Fabian et al. 2009; Zoghbi et al. 2010, 2011). Such strong Fe-K emission requires a high iron abundance to explain. The high iron abundance

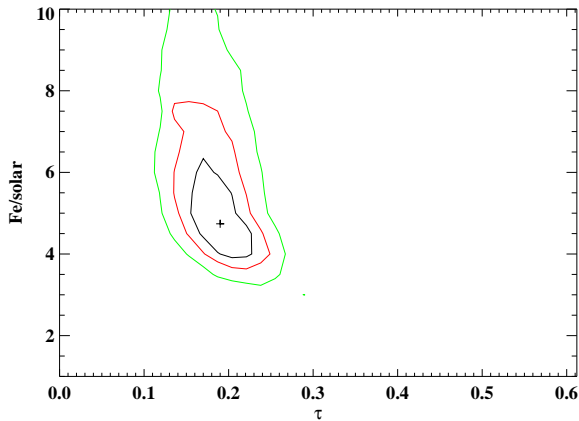


Figure 11. The figure shows the contour plot of the depth of the absorption edge against the iron abundance.

is also the reason why Fe-L emission is seen in the spectrum of 1H0707-495. Nevertheless, the Fe-K line in CBS 126 is not particularly strong, as would be expected if the abundance was indeed > 9 . The Fe-L feature is not present in the soft X-ray spectrum either. Therefore we find it highly unlikely that the source has such high iron abundances. In addition, it is difficult to explain the excess above the powerlaw continuum discovered at low-energies in the difference spectra using model A, as the RMS spectrum suggest that there are no components contributing extra variability in the low-energy band.

Fig. 11 shows the contour plot of iron abundance against the depth of the absorption edge, and contours are plotted at 67%, 90% and 99% levels. The value of iron abundance spans a wide range from 3 to 10 in the contour plot, implying CBS 126 is likely super-solar, but the value of iron abundance is not constrained by the current dataset. We cannot make a correct measurement of the iron abundance yet. However, the Fe-K line presented in the spectrum is not particularly strong, the assumption of solar abundance used in Model B seems to be more reasonable.

4.2 Possibility of the Existence of Warm Absorbers

Both the time-averaged and the time-resolved spectra can be fitted successfully by model B. The absorption edge has an energy of ~ 0.88 keV, close to the O VIII edge and Ne I, Ne II edges (Daltabuit & Cox 1972). The edge is possibly part of the absorption caused by a warm absorber. Moreover, it seems there is a weak absorption line at ~ 6.6 keV (see Fig. 12) with an $EW = -54^{+44}_{-34}$ eV, which may be a Fe XXVI absorption line caused by a highly ionised warm absorber. This kind of warm absorber produces few absorption lines in the low-energy spectra. Therefore the absorption edge at ~ 0.88 keV, if real, is likely caused by a different warm absorber. However, the *Suzaku* XIS does not have enough energy resolution to confirm the existence of warm absorbers. The *Swift* XRT covers soft X-ray energies down to 0.3 keV but does not have enough energy resolution either. A more powerful instrument and an observation with a longer exposure time may be needed to confirm the assumption. Such an observation will also help index the absorption edge.

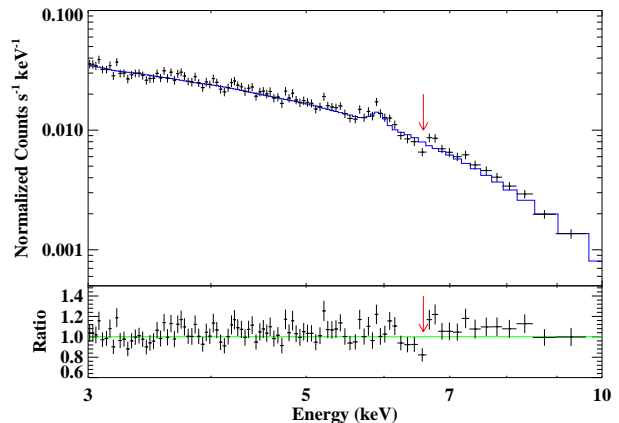


Figure 12. The figure shows the *Suzaku* FI XIS spectrum fitted with model B. The red arrow at ~ 6.6 keV in the figure indicates a possible Fe XXVI absorption line.

4.3 Variation of the Ionisation Parameter

CBS 126 shows enormous variability in long-term X-ray observations (see Fig. 1), and it is also variable in short-term observations like the one discussed in this paper. The time-resolved analysis indicates the ionisation parameter varies with time. The powerlaw component does not vary a lot during the observation, but the ionisation parameter drops significantly in period 3, and it is likely that an increase in the hydrogen number density of the disc or the height of the corona caused the drop in $\xi = L_{ion}/nR^2$. The hydrogen number density of the disc is expected not to change significantly within a short period of time. The RMS spectrum indicates that the disc component does not contribute significant variability. It is more likely that the properties of the accretion disc remain constant. Assuming n remains constant, R needs to increase by a factor of ~ 1.4 between period 2 and 3 in order to explain the drop in ionisation parameter seen here.

As stated in section 3.2.2, different ionisation parameters produce different amount of soft excess. The excess at the soft X-ray band seen in the *Suzaku* difference spectra could be a result of changing ionisation parameter. However, this again needs to be confirmed by a more detailed observation.

5 CONCLUSION

We test the relativistic reflection model on the new X-ray observation carried out in late 2010 of the BLS1 galaxy CBS 126. The spectra show an enormous soft excess in low-energy band, which is difficult to be explained by only the relativistic reflection continuum. An iron abundance larger than 9 times the solar value is needed to produce the soft excess. Based on the information offered by the difference spectra and the RMS spectrum, a multiplicative component such as an absorption edge or a warm absorber is more likely. We find the model composed of a relativistic reflection continuum with solar abundance and an absorption edge (Model B) is preferred. To investigate this further, we carried out a time-resolved analysis to confirm the presence of this feature. Model B which contains an absorption edge and solar abundance fits the time-resolved spectra well. In time-resolved analysis we find the ionisation parameter drops in period 3, and this is probably caused by an increase of the height of the corona. The change in ionisation

parameter might also cause the excess at the low-energy band seen in the difference spectra.

This work shows that the reflection model can be used in interpreting the spectra of a BLS1 galaxy. We note that a strong soft excess does not necessarily imply a strong iron K line in the reflection scenario. We find the edge model explains both the time-averaged and the time-resolved spectra well, and it also interprets what we see in the difference and the RMS spectra. Nevertheless, due to the low signal-to-noise ratio of the data, whether there are warm absorbers in the source cannot be confirmed yet. The absorption edge is most likely an OVIII edge, but the possibility of neon cannot be ruled out. *Suzaku* and *Swift* do not have enough resolving power in the low-energy band. An observation by *Chandra* HETGS or *XMM-Newton* RGS may offer more details in the low-energy spectra. Future observation of the higher energy spectra with NuSTAR or ASTRO-H can test the reflection model.

ACKNOWLEDGEMENTS

RCR is supported by NASA through the Einstein Fellowship Program, grant number PF1-120087. Swift at PSU is supported by NASA contract NAS5-00136. DG acknowledges support by NASA contract NNX07AH67G. ST is supported by NASA Grant NNX10AR32G.

REFERENCES

- Arnaud K. A., 1996, in *Astronomical Society of the Pacific Conference Series*, Vol. 101, *Astronomical Data Analysis Software and Systems V*, G. H. Jacoby & J. Barnes, ed., p. 17
- Boller T., Brandt W. N., Fink H., 1996, *A&A*, 305, 53
- Brandt W. N., Mathur S., Elvis M., 1997, *MNRAS*, 285, L25
- Burrows D. N., Hill J. E., Nousek J. A., Kennea J. A., Wells A., Osborne J. P., Abbey A. F., Beardmore A., Mukerjee K., Short A. D. T., Chincarini G., Campana S., Citterio O., Moretti A., Pagani C., Tagliaferri G., Giommi P., Capalbi M., Tamburelli F., Angelini L., Cusumano G., Bräuninger H. W., Burkert W., Hartner G. D., 2005, *Space Sci. Rev.*, 120, 165
- Cardelli J. A., Clayton G. C., Mathis J. S., 1989, *ApJ*, 345, 245
- Crummy J., Fabian A. C., Gallo L., Ross R. R., 2006, *MNRAS*, 365, 1067
- Daltabuit E., Cox D. P., 1972, *ApJ*, 177, 855
- Done C., Davis S. W., Jin C., Blaes O., Ward M., 2012, *MNRAS*, 420, 1848
- Edelson R., Turner T. J., Pounds K., Vaughan S., Markowitz A., Marshall H., Dobbie P., Warwick R., 2002, *ApJ*, 568, 610
- Fabian A. C., Zoghbi A., Ross R. R., Uttley P., Gallo L. C., Brandt W. N., Blustin A. J., Boller T., Caballero-Garcia M. D., Larsson J., Miller J. M., Miniutti G., Ponti G., Reis R. C., Reynolds C. S., Tanaka Y., Young A. J., 2009, *Nature*, 459, 540
- Gehrels N., Chincarini G., Giommi P., Mason K. O., Nousek J. A., Wells A. A., White N. E., Barthelmy S. D., Burrows D. N., Cominsky L. R., Hurley K. C., Marshall F. E., Mészáros P., Roming P. W. A., Angelini L., Barbier L. M., Belloni T., Campana S., Caraveo P. A., Chester M. M., Citterio O., Cline T. L., Cropper M. S., Cummings J. R., Dean A. J., Feigelson E. D., Fenimore E. E., Frail D. A., Fruchter A. S., Garmire G. P., Gendreau K., Ghisellini G., Greiner J., Hill J. E., Hunsberger S. D., Krimm H. A., Kulkarni S. R., Kumar P., Lebrun F., Lloyd-Ronning N. M., Markwardt C. B., Mattson B. J., Mushotzky R. F., Norris J. P., Osborne J., Paczynski B., Palmer D. M., Park H.-S., Parsons A. M., Paul J., Rees M. J., Reynolds C. S., Rhoads J. E., Sasseen T. P., Schaefer B. E., Short A. T., Smale A. P., Smith I. A., Stella L., Tagliaferri G., Takahashi T., Tashiro M., Townsley L. K., Tueller J., Turner M. J. L., Vietri M., Voges W., Ward M. J., Willingale R., Zerbi F. M., Zhang W. W., 2004, *ApJ*, 611, 1005
- Gierliński M., Done C., 2004, *MNRAS*, 349, L7
- , 2006, *MNRAS*, 371, L16
- Godet O., Beardmore A. P., Abbey A. F., Osborne J. P., Cusumano G., Pagani C., Capalbi M., Perri M., Page K. L., Burrows D. N., Campana S., Hill J. E., Kennea J. A., Moretti A., 2009, *A&A*, 494, 775
- Grupe D., Beuermann K., Thomas H.-C., Mannheim K., Fink H. H., 1998a, *A&A*, 330, 25
- Grupe D., Komossa S., Leighly K. M., Page K. L., 2010, *ApJS*, 187, 64
- Grupe D., Thomas H.-C., Beuermann K., 2001, *A&A*, 367, 470
- Grupe D., Wills B. J., Leighly K. M., Meusinger H., 2004, *AJ*, 127, 156
- Grupe D., Wills B. J., Wills D., Beuermann K., 1998b, *A&A*, 333, 827
- Hill J. E., Burrows D. N., Nousek J. A., Abbey A. F., Ambrosi R. M., Bräuninger H. W., Burkert W., Campana S., Cheruvu C., Cusumano G., Freyberg M. J., Hartner G. D., Klar R., Mangels C., Moretti A., Mori K., Morris D. C., Short A. D. T., Tagliaferri G., Watson D. J., Wood P., Wells A. A., 2004, in *Society of Photo-Optical Instrumentation Engineers (SPIE) Conference Series*, Vol. 5165, *Society of Photo-Optical Instrumentation Engineers (SPIE) Conference Series*, K. A. Flanagan & O. H. W. Siegmund, ed., pp. 217–231
- Jin C., Ward M., Done C., Gelbord J., 2012, *MNRAS*, 420, 1825
- Miniutti G., Fabian A. C., 2004, *MNRAS*, 349, 1435
- Mitsuda K., Inoue H., Koyama K., Makishima K., Matsuoka M., Ogawara Y., Suzuki K., Tanaka Y., Shibasaki N., Hirano T., 1984, *PASJ*, 36, 741
- Poole T. S., Breeveld A. A., Page M. J., Landsman W., Holland S. T., Roming P., Kuin N. P. M., Brown P. J., Gronwall C., Hunsberger S., Koch S., Mason K. O., Schady P., vanden Berk D., Blustin A. J., Boyd P., Broos P., Carter M., Chester M. M., Cucchiara A., Hancock B., Huckle H., Immler S., Ivanushkina M., Kennedy T., Marshall F., Morgan A., Pandey S. B., de Pasquale M., Smith P. J., Still M., 2008, *MNRAS*, 383, 627
- Pounds K. A., Done C., Osborne J. P., 1995, *MNRAS*, 277, L5
- Puchnarewicz E. M., Mason K. O., Cordova F. A., Kartje J., Brabduardi A. A., Puchnarewicz E. M., Mason K. O., Cordova F. A., Kartje J., Branduardi-Raymont G., Mittaz J. P. D., Murdin P. G., Allington-Smith J., 1992, *MNRAS*, 256, 589
- Reis R. C., Fabian A. C., Reynolds C. S., Brenneman L. W., Walton D. J., Trippe M., Miller J. M., Mushotzky R. F., Nowak M. A., 2012, *ApJ*, 745, 93
- Roming P. W. A., Kennedy T. E., Mason K. O., Nousek J. A., Ahr L., Bingham R. E., Broos P. S., Carter M. J., Hancock B. K., Huckle H. E., Hunsberger S. D., Kawakami H., Killough R., Koch T. S., McLelland M. K., Smith K., Smith P. J., Soto J. C., Boyd P. T., Breeveld A. A., Holland S. T., Ivanushkina M., Pryzby M. S., Still M. D., Stock J., 2005, *Space Sci. Rev.*, 120, 95
- Roming P. W. A., Koch T. S., Oates S. R., Porterfield B. L., Vanden Berk D. E., Boyd P. T., Holland S. T., Hoversten E. A., Immler S., Marshall F. E., Page M. J., Racusin J. L., Schneider D. P., Breeveld A. A., Brown P. J., Chester M. M., Cucchiara A.,

- DePasquale M., Gronwall C., Hunsberger S. D., Kuin N. P. M., Landsman W. B., Schady P., Still M., 2009, *ApJ*, 690, 163
- Ross R. R., Fabian A. C., 2005, *MNRAS*, 358, 211
- Schlegel D. J., Finkbeiner D. P., Davis M., 1998, *ApJ*, 500, 525
- Schurch N. J., Done C., 2007, *MNRAS*, 381, 1413
- Shen Y., Richards G. T., Strauss M. A., Hall P. B., Schneider D. P., Snedden S., Bizyaev D., Brewington H., Malanushenko V., Malanushenko E., Oravetz D., Pan K., Simmons A., 2011, *ApJS*, 194, 45
- Titarchuk L., 1994, *ApJ*, 434, 570
- Voges W., Aschenbach B., Boller T., Bräuninger H., Briel U., Burkert W., Dennerl K., Englhauser J., Gruber R., Haberl F., Hartner G., Hasinger G., Kürster M., Pfeffermann E., Pietsch W., Predehl P., Rosso C., Schmitt J. H. M. M., Trümper J., Zimmermann H. U., 1999, *A&A*, 349, 389
- Wilms J., Allen A., McCray R., 2000, *ApJ*, 542, 914
- Zoghbi A., Fabian A. C., Uttley P., Miniutti G., Gallo L. C., Reynolds C. S., Miller J. M., Ponti G., 2010, *MNRAS*, 401, 2419
- Zoghbi A., Uttley P., Fabian A. C., 2011, *MNRAS*, 412, 59